Materials Research. 2023; 26(suppl. 1):e20230055
DOI: https://doi.org/10.1590/1980-5373-MR-2023-0055

Selective Laser Melting of Ti-6Al-4V Alloy: Correlation Between Processing Parameters, Microstructure and Corrosion Properties

Marcio Sangali*[a], *Alessandra Cremasco*[b], *Juliano Soyama*[a], *Rubens Caram*[a], *Rodrigo J. Contieri*[b]

[a]*Universidade Estadual de Campinas, Faculdade de Engenharia Mecânica, Campinas, SP, Brasil.*
[b]*Universidade Estadual de Campinas, Faculdade de Ciências Aplicadas, Campinas, SP, Brasil.*

Received: January 16, 2023; Revised: April 17, 2023; Accepted: May 21, 2023

Additive Manufacturing technology has continually advanced, allowing microstructure and property optimization. In recent years, several studies have been carried out with the aim of understanding mechanisms of formation and evolution of the microstructure and, consequently, their influence on mechanical properties. However, correlations between microstructure and corrosion properties are not completely understood, making more systematic investigations necessary. In this work, samples of the Ti-6Al-4V alloy were produced by combining different laser powers and scanning speeds in order to generate different energy density values (VED) with subsequent microstructures and properties. The samples were characterized by optical and scanning electron microscopy, hardness and relative density. Complementarily, corrosion tests were carried out. For the entire set of parameters used, the processed samples showed the formation of acicular martensite α′, followed by different levels of porosity depending on the applied energy density. VED proved to be an important control parameter, and the best combinations of hardness and corrosion resistance were obtained for the parameter ratio that generated energy densities greater than 100 J/mm^3.

Keywords: *Additive Manufacturing, Titanium Alloys, Ti-6Al-4V, Laser Powder Bed Fusion (L-PBF).*

1. Introduction

Over the last few years, titanium and its alloys have been widely used in a broad range of applications, which is due to their unique properties such as low density, high strength, low elastic modulus, excellent biocompatibility, and high corrosion resistance[1-3]. Consequently, Ti-based products find their way into several fields in the medical and healthcare industry. The demand for biomaterials has increased dramatically in recent decades, especially for the use of Ti alloys, largely due to the increase in life expectancy, often accompanied by bone diseases such as osteoporosis. Still, regardless of age, fractures or injuries from traffic accidents, or the practice of high-impact sports also contributes to the increase in demand for metallic biomaterials[4,5].

A report recently published by the Mordor Intelligence Agency on the global biomaterials market assessed the possibility of growth for the period between 2022 and 2027[6]. The study identified North America and Asia-Pacific as the most significant markets for the industry with the fastest-growing trends. It also indicates an annual growth rate (CAGR) of 13.69%, which represents a considerable amount of annual return on investment. In this sense, such trends and information are valuable and motivating for researchers and orthopedic implant sectors to allocate efforts and resources, whether developing or improving metallic biomaterials and processes.

The techniques commonly applied in the manufacturing of metallic implants, mostly using Ti alloys, require many complex steps, which invariably increase the cost of production and, hence, the final product. Unfavorably, such manufacturing techniques generate large amounts of material waste, high energy consumption, and production time, further contributing to rising costs[7,8]. On the other hand, manufacturing processes using additive manufacturing (AM) techniques enable to produce complex shaped parts in fewer steps or reprocessing, with high precision and much less material waste. Therefore, they make it possible to mitigate manufacturing and final product costs, in addition to positively implementing aspects regarding sustainability and the use of new materials[7,9-11].

Within the context of Ti alloys and implant manufacturing, additive manufacturing (AM) technology offers new opportunities to produce metallic components. One of the main AM techniques is the laser powder bed fusion (L-PBF), also known as selective laser melting (SLM). This technique has gained great prominence in recent decades[12-21]. The L-PBF process relies on layer-by-layer construction, using a laser beam to selectively melt and sinter metallic powders[12]. The thickness of each layer defines the resolution of the formed solid. However, being one of the process parameters, the variation in the thickness of each layer will result in different properties of the material. The thickness of each

*e-mail: contieri@unicamp.br

layer can be changed according to the type of raw material used and the power of the heat source responsible for its melting. Each type of material processed requires different process parameters to obtain the desired specifications. Additionally, the scanning speed and the hatch spacing drastically influence the final part. All parameters used can be correlated through the generated volumetric energy density (VED)[22], which is the principal normalized indicator applied, even knowing that variations exist from equipment to equipment, as well as from raw material[23]. The VED value is determined using equation: $VED = P \quad V \cdot L \cdot H$, where P, V, L and H are respectively, the laser power (W), scanning speed (mm/s), layer thickness (mm) and hatch spacing (mm).

SLM technology has been continually modernized, allowing microstructure and property optimization. When it comes to Ti alloys, the Ti-6Al-4V alloy is the most used and studied metallic material concerning additive manufacturing, being one of the focuses of this work. In recent years, several studies have been carried out to understand the Ti-6Al-4V microstructure evolution and, consequently, its influence on the mechanical properties of additively manufactured components.

Studies reported by Murr and co-authors point out that due to the high cooling rates imposed, the main microstructure formed is the acicular martensite α´[24]. Consequently, alloys produced by SLM have high mechanical strength, followed by low elongation. However, despite the low ductility, the elongation can be reasonably improved by re-processing using such as annealing heat treatments or Hot Isostatic Pressing (HIP), as commonly applied in powder metallurgy processes[25]. According to a critical review on additive manufacturing of Ti-6Al-4V alloy reported by Nguyen et al.[26], as-built or post-processed parts can reach yield strength values between 700 MPa and 1270 MPa, with elongation in the range of 2 to 20%, depending on the applied process parameters.

On the other hand, the corrosion behavior of Ti alloys processed by AM has been superficially studied concerning construction orientation relationships, or as a complementary analysis of the results of mechanical properties resulting from simple alloys or the compositional variation within a given system, by several researchers[27-43]. However, the correlations between microstructure and corrosion resistance are not completely understood, making more systematic investigations necessary. To directly investigate this essential question, from different combinations of processing parameters and, consequently, microstructures and defects, systematic conditions were generated to understand the corrosion resistance in as-built samples.

2. Experimental Procedure

The Ti-6Al-4V (wt.%) samples were prepared from gas atomized powder (grade 5, 15-45 μm) using a OmniSint-160 (OmniTek Company) L-PBF machine equipped with Yb:YAG fiber laser, wavelength of 1070 nm, spot size of 80 μm and maximum laser power of 400 W. The depositions were carried out using high-purity Ar. The oxygen content in the sintering chamber was found to be less than 550 ppm. A substrate made up of Ti-6Al-4V alloy was employed to produce the samples. All the experiments were performed applying laser power (P) between 100 W and 232 W, scanning speed (V) from 600 mm/s to 1200 mm/s, hatch spacing (H) of 70 μm, and layer thickness (L) of 30 μm. The laser scanning direction was rotated between every deposited layer by 67°. Cylinders 10 mm in diameter and 5 mm in height, in total 28 specimens, were manufactured with different process parameters and, consequently, energy density. The relative density of samples produced by L-PBF was evaluated using the Archimedes Method, in accordance with ASTM Standard[44]. Image analyzes were also used in order to compare the porosity[45,46]. The analysis of the porosity was carried out using digital image processing through the Image J software. The level of the segmentation (threshold) that indicated the porosity was demarcated and from that, through a standard routine of the software, the percentage of porosity was calculated. For this analysis, at least five images from different regions were used.

The samples were subject to conventional metallographic preparation etched with a Kroll's solution (50 mL of HNO_3, 10 mL of HF, and 100 mL of H_2O). The microstructures were evaluated employing stereo (Olympus SZ61) and conventional (Olympus BX60M) optical microscope and, scanning electron microscopy (SEM) on Zeiss EVO MA15 equipment. Vickers hardness was evaluated on a Buehler 2100 hardness tester. For each sample, ten measurements were performed with loads of 200 gf for 15 seconds. The samples' chemical composition was determined by X-ray fluorescence (XRF) using a Shimadzu EDX-7000 Spectrometer and energy-dispersive X-ray spectroscopy (SEM-EDS), while the interstitial O and N contents were measured on a Leco TC400 analyzer, with results listed on Table 1.

The electrochemical corrosion behavior was studied by polarization potentiodynamic tests in a potentiostat/galvanostat (PGSTAT302N - Metrohm Autolab) after 1 h of stabilization open circuit potential (OCP) using a three-electrode cell constituted by a platinum rod as counter-electrode (CE), an Ag/AgCl (3M KCl) electrode as reference (RE) and Ti-6Al-4V samples printed as working electrode (WE). The 0.9% NaCl solution naturally aerated at room temperature was used as an electrolyte and the surface area exposed was 0.6 cm^2. The potential range evaluated was -0.800 mV up to 2.800 mV vs. (OCP) using a scanning rate of 0.167 mV/s. Prior to corrosion tests, the samples were prepared by grinding using a 1200-grit SiC wet sandpaper and ultrasonically cleaned in alcohol for 3 min, and dry using nitrogen flow. The corrosion potential (E_{corr}) and corrosion density current (i_{corr}) were obtained by Tafel extrapolation from the recorded polarization curves. After corrosion tests, the sample surfaces were observed in a tabletop SEM (TM1000, Hitachi) to check the possible pit corrosion. Triplicate potentiodynamic tests were carried

Table 1. Samples' chemical composition (wt. %)

	Ti	Al	V	O	N
Ti-6Al-4V	Balance	5.6+0.3	3.8+0.6	0.160+0.005	0.04+0.01

out and the corrosion resistance parameters (E_{corr} and i_{corr}) were obtained from the average of three registered curves.

3. Results and Discussion

To understand more systematically the effects of microstructure and defects on corrosion properties, the 28 samples processed via SLM were investigated using a combination of scanning speed and laser power parameters. Figure 1 presents the compilation of these results from the processing maps for energy density and densification.

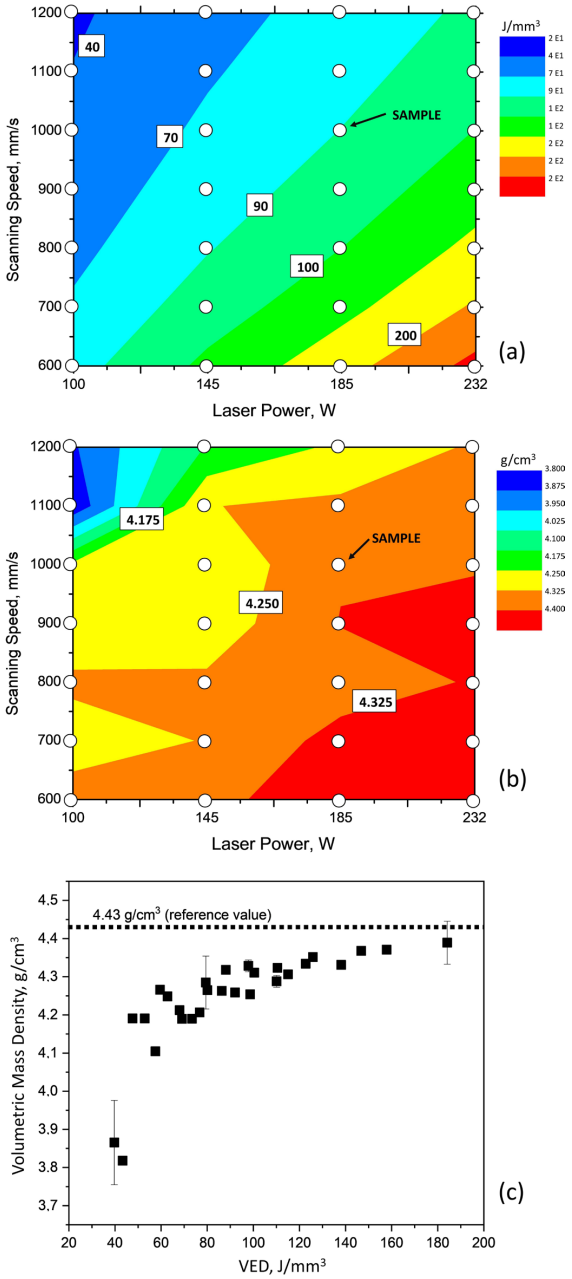

Figure 1. Process maps for Ti-6Al-4V by L-PBF: (a) VED and (b) volumetric mass density due to scanning speed versus Laser power parameters, and (c) volumetric mass density as a function of VED.

According to Figure 1, there was a clear relationship between the applied volumetric energy density and the sample densification. Lower levels of VED, below 70 J/mm³, provided the lowest density values, 4.175 g/cm³. Drastic density reduction occurs when laser power is below 145 W and scanning speed is above 1000 mm/s, respectively. On the other hand, the highest values of densification, above 4.325 g/cm³, appear for VED greater than 100 J/mm³, implemented from powers above 185 W and scanning speeds below 900 mm/s. Luo et al.[47] conducted a parameter investigation of the L-PBF applied to the Ti-6Al-4V alloy. The authors showed similar results with porosity in the range of 1.0 - 2.5% in the case of comparable scan speeds and laser power. However, the VED was significantly lower between 60 - 80 J/mm³. A high VED can be associated with the keyholing effect, which was not observed in this study. Figure 1c shows the Volumetric Mass Density as a function of VED. As reported previously[48-50], low VED led to less densification but there was a fast increase in the density for higher VED values. Moreover, from approximately 120 J/mm³, the density stabilized at about 4.35 g/cm³, which supports the optimum parameter for higher VED values in the case of the investigated conditions. For comparison and calculations of density and porosity, the density of 4.43 g/cm³ of Ti-6Al-4V was used.

Figure 2 shows the correlation between the porosity percentage and the applied laser power. The results suggested that porosity decreased as laser power increased, regardless of the scanning speed. The decay of the relative porosity shows a greater tendency to decrease when the speed was increased. For lower speeds, below 900 mm/s, this effect was less pronounced. However, the lowest porosity was found for the highest power value and lowest speed, 232 W and 600 mm/s, respectively. In a study related to the Ti-6Al-4V alloy processed by L-PBF, Gong et al.[51] reported that porosity was not linearly related to energy density. However, high and low energy densities (120 and 20 J/mm³) led to porosities of less than 15%. On the other hand, Promoppatum et al.[52] investigated porosity formation in Ti-6Al-4V produced by L-PBF and reported a constant nearly zero porosity for energy densities above 40 J/mm³.

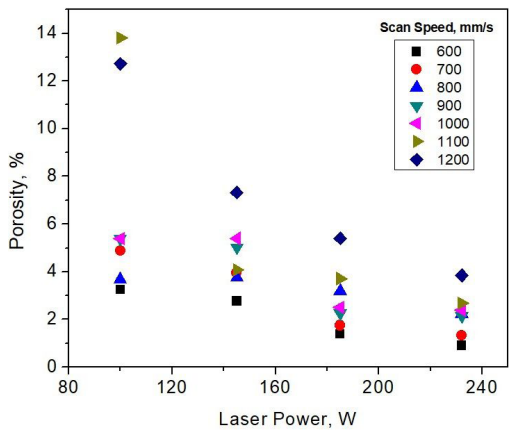

Figure 2. Relationship between porosity percentage and laser power relative to different scanning speeds of samples processed by L-PBF.

Figure 3 shows the results obtained from microhardness tests. When applying power higher than 142 W, its effects on the hardness become less evident, since those values approach a plateau, regardless of the scanning speed. As the power increases, the plotted points become more overlapping. The hardness is associated with microstructural refinement, which is relative to the cooling rate. Higher powers attenuate the heat extraction imposed by the scanning speed to the same value. On the other hand, lower laser power results in less heat input, favoring more effective cooling and, consequently, higher microstructural refinement. Khorasani et al.[53], based on statistical analyses, suggested that low values of hardness (and density) seem to be governed by low VED. The low energy input results in little energy transfer to the weld pool and, consequently, low processing temperature. Therefore, this phenomenon provides incomplete melting and porosity formation, explaining the different behavior.

From the established pre-analyses, the best conditions were chosen, and the best values obtained regarding densification, volumetric energy density, and hardness, in a wide range of scanning speed, were selected. At this point, Figure 4 presents the results of optical and scanning electron microscopy of samples with laser power of 232 W and scanning speed varying between 600 and 1200 mm/s, in a total of seven conditions. From the Stereo OM images inserted in Figure 4 (first column), even when the best parameters are selected, there is still a significant effect on porosity. It is noticed that the porosity level increased with the scanning speed values. Image analysis showed that the porosity values were very close to those observed by the Archimedes method. The lowest and highest values found for porosity were 0.99% and 4.21% respectively for the speeds of 600 mm/s and 1200 mm/s. Therefore, even for high VED values, it was still possible to observe the presence of pores. In the same way as observed by Gong et al.[51], that porosity was not linearly related to the energy density. However, when observing the behavior based on the difference between the VED values (Figure 1), even for values greater than 90 J/mm^3, it is possible to attribute the increase in the amount of pores to differences between the VED values. It can be seen in the left column (Figure 4), that above 900 mm/s the porosity level

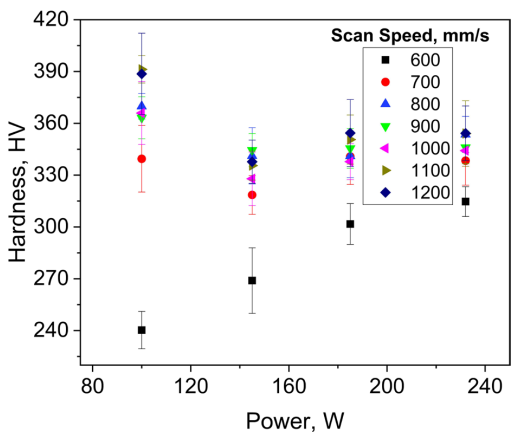

Figure 3. Relationship between Vickers hardness and laser power relative to different scanning speeds of samples processed by L-PBF.

becomes more pronounced. When the VED value decreased by around 30% (122 J/mm^3) from the maximum, the porosity increased. Thus, even small fluctuations in energy (VED) can modify the heat transfer conditions and, consequently, change the amount of pores and densification.

The OM (200X) and SEM (5kX) micrographs obtained after L-PBF process is shown in two columns on the right side of Figure 4. The microstructures are made up of acicular α′ martensitic for all analyzed scanning speeds. As observed in the literature, no significant evidence of β phase was found. Since the process takes place at elevated temperatures, the heating of Ti-6Al-4V above the β transus temperature changed its crystal structure from HCP to BCC. Consequently, the rapid cooling imposed by the processing leads to the formation of martensitic α', which is thermodynamically unstable. At low magnification, through MO images, it can be seen differences in the refinement and length of the α′ laths. Specifically, we observed that higher scanning speeds and higher VED values resulted in more pronounced microstructural refinement, accompanied by a decrease in grain size. Such results are consistent with the literature. Javidrad and Salemi[54] also the refinement of alpha laths to increased energy, but they did not systematize setting parameters or observe them independently. Figure 4 clearly indicates that the scanning speed has a significant impact on microstructural refinement, corroborating with previous discussions (Figure 3). Comparing the lowest and highest scanning speeds applied, we can see a relative reduction in the length of the alpha laths by approximately 70%. For higher magnifications, it was found that the behavior, as observed for porosity, changed for scanning speed greater than 900 mm/s, promoting a more refined microstructure concerning the acicular martensite needles. It is a general observation in solidification processing that increasing the cooling rates leads to microstructural refinement. According to Yang et al.[55], martensite size can be controlled by varying the L-PBF processing parameters such as hatch spacing and scanning speed. Severe change from 600 mm/s to 1100 mm/s showed that the martensite size decreased significantly, similar to the behavior observed in the present analyses.

Figure 5a shows the polarization curves of samples Ti-6Al-4V processed with different porosity levels resulting from the scanning speeds employed. Overlapping of Tafel curves in cathodic and anodic branches was observed, which indicated similar corrosion behavior for the investigated alloys. Although the acicular martensite α' volume fraction and microstructural refinement were slightly different, a similar corrosion behavior could be expected due to identical chemical composition and phase combinations. The E_{corr} e i_{corr} were determined by the linear fitting of Tafel curves and the results are shown in Table 2. The samples printed using scanning speed of 1000 mm/s showed the highest E_{corr} (- 570 mV) and lowest i_{corr} (140 nA/cm^2). A greater value of E_{corr} indicates the formation of a more stable passive film, while a lower i_{corr} means easy passivation of the exposed surface[56].

The commercial Grade 5 Ti-6Al-4V processed by conventional route typically shows a biphasic microstructure formed by α + β phases. The same alloy produced by L-PBF generates a columnar prior β phase combined with higher content of the acicular α' phase. The role of microstructure of Ti-6Al-4V on corrosion resistance is controversial. While some works attribute the lower corrosion behavior to acicular α', it has higher energy state in

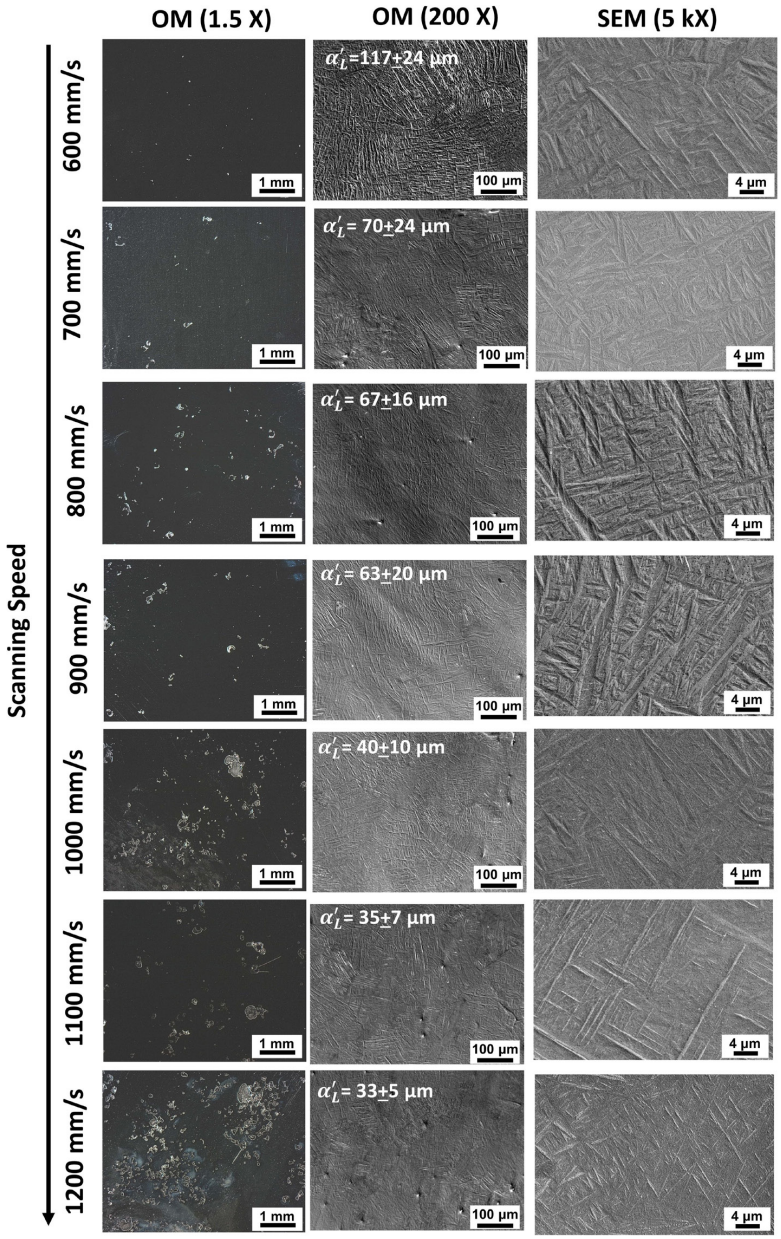

Figure 4. Images obtained from samples processed with laser power fixed at 232 W and with different scanning speeds. The first column on the left side corresponds to OM images (stereo microscope, 1.5X), showing porosity whereas the columns on the right side the OM and SEM microstructure of the cross-section. The length of the α' laths is shown in the figure (α'_L).

Table 2. Experimental corrosion parameters for different porosity levels of Ti-6Al-4V processed by SLM.

Scanning Speed (mm/s)	Porosity density (%)	E_{corr} (mV)	i_{corr} (nA/cm^2)	E_{pp} (mV)	i_{pp} (µA/cm^2)
600	0.90	-664.43	291.58	-131.11	3.62
700	1.32	-650.01	209.67	-54.58	3.98
800	2.21	-613.24	184.72	-53.66	4.71
900	2.14	-570.49	234.47	-81.86	4.50
1000	2.39	-570.21	140.42	-	-
1100	2.67	-629.86	220.53	-	-
1200	3.85	-606.79	467.27	-	-

corrosion and dissolves easier in a corrosive media[57,58], others take in that the homogeneous distribution of alloying elements on hexagonal martensite has a beneficial effect to corrosion, reducing the susceptibility to localized attack[59]. In the same way, a decreasing the stable β phase volume fraction caused by the melting and solidification stages in additive manufacturing can results in inferior corrosion resistance when compared to samples produced by a conventional processing route[60] and therefore, the β-phase enhances the resistance to charge transfer and reduces the metal dissolution rate[42], as also a poor corrosion resistance can are associated to more interfacial regions in a α+β microstructure that result in a native titanium oxide film less homogeneous[59].

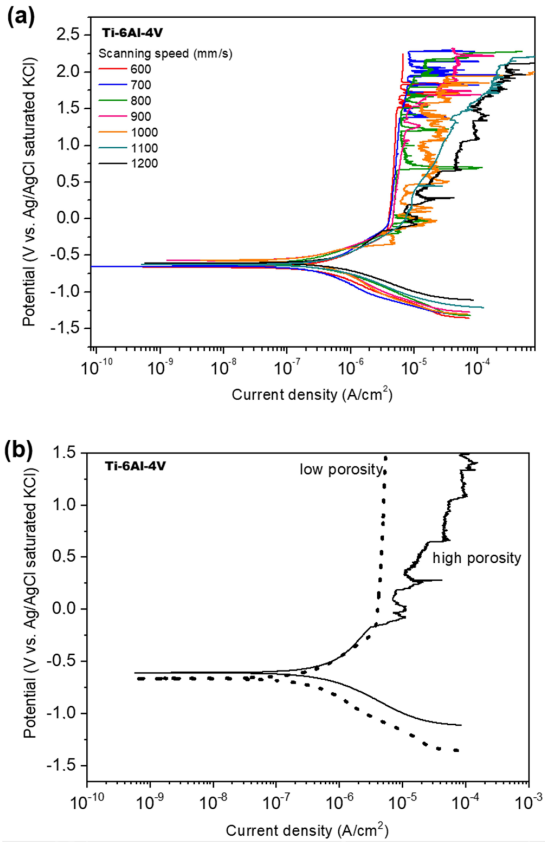

Figure 5. (a) Polarization curves of Ti-6Al-4V processed by L-PBF and showing different porosity levels in 0.9% NaCl electrolyte at room temperature and, (b) comparison of polarization curves of samples with lower and higher porosity.

On the other hand, the passivation region observed in the samples printed at the lowest scanning speed (600 mm/s) was more stable and comparable to the samples printed using the higher scanning speeds due to their reduced porosity level. In Ti alloys, higher porosity and unequal distribution and irregular shapes of pores result in a fluctuation in polarization curves due to oscillation of current density showing a passive film less stable, albeit it can be quickly repassivated by its excellent repair ability[42]. Also, this surface porosity inherent of additive manufacturing process conditions can act as crevices, which inside pores the acidification of electrolyte creates a more aggressive environment potentializing the corrosive attack[61,62]. The passive performance of samples is often evaluated by passive current density (ipp) and passive potential (Epp), in which the lower values represent a lower dissolution rate and easier passivation, respectively[42]. This processing condition of 600 mm/s showed lower values of E_{pp} and i_{pp}. In the samples printed using higher scanning speed (from 1000 to 1200 mm/s), no clear passivation region was visible on polarization curves and i_{pp} and E_{pp} values were not possible to be determined due to a continuous pitting formation and subsequent repassivation design as metastable pitting[29] possibly associated to crevice corrosion[61]. Poor corrosion resistance with increasing scanning speeds at a constant laser power was verified by Naidoo et al.[40] in a Ti-Al-Si-Cu/Ti-Al-V composite produced by laser metal deposition, as also observed in this paper. A comparison of polarization curves of samples processed by L-PBF with lower and higher porosity levels is shown in Figure 5b.

Figure 6 displays the SEM images of Ti-6Al-4V samples processed by L-PBF with scanning speed that resulted in lower (Figure 6a) and higher (Figure 6b) porosity levels.

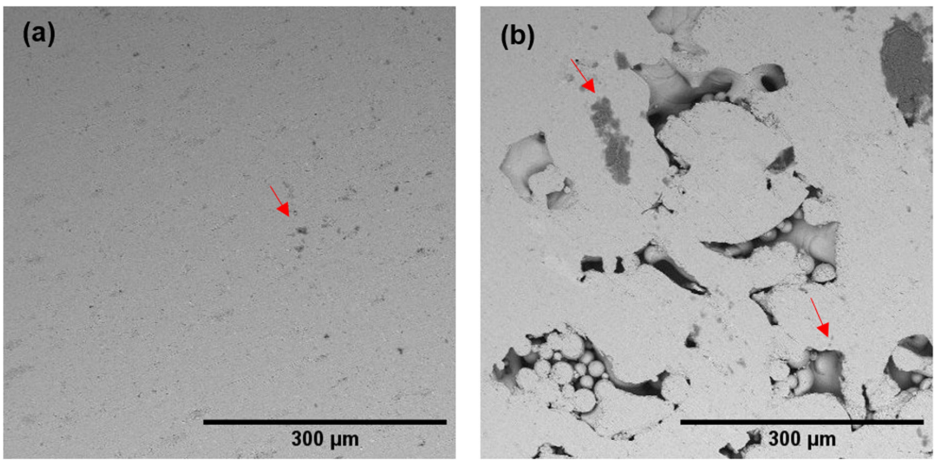

Figure 6. SEM-Images of Ti-6Al-4V processed by L-PBF with speed scanning of (a) 600 mm/s and (b) 1200 mm/s after polarization tests in 0.9% NaCl electrolyte at room temperature.

The images were recorded after polarization tests in 0.9% NaCl solution to observe any pitting corrosion. As observed, both samples show corrosion products on surfaces, with pits coupled to pores observed more remarkably on samples processed with higher scanning speed and high porosity.

4. Conclusions

In this paper, the effects of different processing parameters in the manufacturing of the Ti-6Al-4V alloy by the L-PBF technique on the microstructure and corrosion properties were systematically examined and analyzed. Thus, under the conditions of this study, the following conclusion can be drawn: (1) The VED parameter proved to be very sensitive to obtaining high-density specimens when using high laser powers. The highest densification found was 99.01% (99.10% Archimedes) with 184 J/mm^3 from 600 mm/s and 232 W of power; (2) For VED values greater than 100 J/mm^3 with a power of 232 W, the average hardness was 330 HV, higher than the lowest ranges of energy density; (3) Regardless of the processing conditions, specimens were obtained with a final acicular martensite α′ microstructure with greater microstructural refinement from 900 mm/s (232 W); (4) The different levels of porosity and pore morphology generated fluctuations on polarization curves due to oscillation of current density showing a passive film less stable. The best processing condition occurred at 184 J/mm^3 resulting from 600 mm/s and 232 W resulting in a more stable passivation film.

5. Acknowledgements

The authors thank the Brazilian research agencies, FAPESP (State of São Paulo Research Foundation, Grant #2018/18293-8) and CNPq (National Council for Scientific and Technological Development, Grant # 407412/2018-2).

6. References

1. Semiatin SL. An overview of the thermomechanical processing of α/β titanium alloys: current status and future research opportunities. Metall Mater Trans, A Phys Metall Mater Sci. 2020;51(6):2593-625. http://dx.doi.org/10.1007/s11661-020-05625-3.
2. Chen LY, Cui YW, Zhang LC. Recent development in beta titanium alloys for biomedical applications. Metals. 2020;10(9):1-29.
3. Zhou D, Zeng W, Xu J, Wang S, Chen W. Evolution of equiaxed and lamellar α during hot compression in a near alpha titanium alloy with bimodal microstructure. Mater Charact. 2019;151:103-11. http://dx.doi.org/10.1016/j.matchar.2019.03.005.
4. Elani HW, Starr JR, Silva JD, Gallucci GO. Trends in dental implant use in the U.S., 1999-2016, and projections to 2026. J Dent Res. 2018;97(13):1424-30. http://dx.doi.org/10.1177/0022034518792567.
5. United Nations Department of Economic and Social Affairs. World population ageing 2020: highlights. New York: United Nations Department of Economic and Social Affairs; 2020. 47 p. https://doi.org/10.18356/9789210051934.
6. Mordor Intelligence [homepage on the Internet]. Hyderabad: Mordor Intelligence; c2022 [cited 2023 May 21]. Available from: https://www.mordorintelligence.com/industry-reports/biomaterials-market
7. Javaid M, Haleem A, Singh RP, Suman R, Rab S. Role of additive manufacturing applications towards environmental sustainability. Adv Ind Eng Polym Res. 2021;4(4):312-22. http://dx.doi.org/10.1016/j.aiepr.2021.07.005.
8. Paris H, Mokhtarian H, Coatanéa E, Museau M, Ituarte IF. Comparative environmental impacts of additive and subtractive manufacturing technologies. CIRP Ann. 2016;65(1):29-32.
9. Baumers M, Tuck C, Bourell DL, Sreenivasan R, Hague R. Sustainability of additive manufacturing: measuring the energy consumption of the laser sintering process. Proc Inst Mech Eng, B J Eng Manuf. 2011;225(12):2228-39.
10. Verma A, Rai R. Sustainability-induced dual-level optimization of additive manufacturing process. Int J Adv Manuf Technol. 2017;88(5-8):1945-59. http://dx.doi.org/10.1007/s00170-016-8905-9.
11. Yang Y, Li L, Pan Y, Sun Z. Energy consumption modeling of stereolithography-based additive manufacturing toward environmental sustainability. J Ind Ecol. 2017;21:S168-78.
12. Agapovichev A, Sotov A, Kokareva V, Smelov V. Possibilities and limitations of titanium alloy additive manufacturing. MATEC Web Conf. 2018;224:01064.
13. Attaran M. The rise of 3-D printing: the advantages of additive manufacturing over traditional manufacturing. Bus Horiz. 2017;60(5):677-88. http://dx.doi.org/10.1016/j.bushor.2017.05.011.
14. Bandyopadhyay A, Traxel KD, Lang M, Juhasz M, Eliaz N, Bose S. Alloy design via additive manufacturing: advantages, challenges, applications and perspectives. Mater Today. 2022;52:207-24. http://dx.doi.org/10.1016/j.mattod.2021.11.026.
15. Davis R, Singh A, Jackson MJ, Coelho RT, Prakash D, Charalambous CP et al. A comprehensive review on metallic implant biomaterials and their subtractive manufacturing. Int J Adv Manuf Technol. 2022;120(3-4):1473-530. http://dx.doi.org/10.1007/s00170-022-08770-8.
16. Gao W, Zhang Y, Ramanujan D, Ramani K, Chen Y, Williams CB et al. The status, challenges, and future of additive manufacturing in engineering. CAD Comput Aided Des. 2015;69:65-89. http://dx.doi.org/10.1016/j.cad.2015.04.001.
17. Grover T, Pandey A, Kumari VST, Awasthi A, Singh B, Dixit P et al. Role of titanium in bio implants and additive manufacturing: an overview. Mater Today Proc. 2020;26:3071-80. http://dx.doi.org/10.1016/j.matpr.2020.02.636.
18. Guo AXY, Cheng L, Zhan S, Zhang S, Xiong W, Wang Z et al. Biomedical applications of the powder-based 3D printed titanium alloys: a review. J Mater Sci Technol. 2022;125:252-64. http://dx.doi.org/10.1016/j.jmst.2021.11.084.
19. Klahn C, Leutenecker B, Meboldt M. Design strategies for the process of additive manufacturing. Procedia CIRP. 2015;36:230-5. http://dx.doi.org/10.1016/j.procir.2015.01.082.
20. Kolomiets A, Popov VV Jr, Strokin E, Muller G, Kovalevsky A. Benefits of titanium additive manufacturing for industrial design development. Trends, limitations and applications. Global J Res Eng. 2018 [cited 2023 May 21];18(2):1-9. https://globaljournals.org/GJRE_Volume18/1-Benefits-of-Titanium.pdf
21. Pérez M, Carou D, Rubio EM, Teti R. Current advances in additive manufacturing. Procedia CIRP. 2020;88:439-44. http://dx.doi.org/10.1016/j.procir.2020.05.076.
22. Patterson AE, Chadha C, Jasiuk IM, Allison JT. Fracture testing of polymer materials processed via fused filament fabrication: a survey of materials, methods, and design applications. Prog Addit Manuf. 2021;6(4):765-80. http://dx.doi.org/10.1007/s40964-021-00196-0.
23. Alinaghian I, Honarpisheh M, Amini S. The influence of bending mode ultrasonic-assisted friction stir welding of Al-6061-T6 alloy on residual stress, welding force and macrostructure. Int J Adv Manuf Technol. 2018;95(5-8):2757-66.
24. Murr LE, Quinones SA, Gaytan SM, Lopez MI, Rodela A, Martinez EY et al. Microstructure and mechanical behavior of Ti-6Al-4V produced by rapid-layer manufacturing, for biomedical

applications. J Mech Behav Biomed Mater. 2009;2(1):20-32. http://dx.doi.org/10.1016/j.jmbbm.2008.05.004.
25. Liverani E, Lutey AHA, Ascari A, Fortunato A. The effects of hot isostatic pressing (HIP) and solubilization heat treatment on the density, mechanical properties, and microstructure of austenitic stainless steel parts produced by selective laser melting (SLM). Int J Adv Manuf Technol. 2020;107(1-2):109-22.
26. Nguyen HD, Pramanik A, Basak AK, Dong Y, Prakash C, Debnath S et al. A critical review on additive manufacturing of Ti-6Al-4V alloy: microstructure and mechanical properties. J Mater Res Technol. 2022;18:4641-61. http://dx.doi.org/10.1016/j.jmrt.2022.04.055.
27. Chen W, Xiao B, Xu L, Han Y, Zhao L, Jing H. Additive manufacturing of martensitic stainless steel matrix composites with simultaneously enhanced strength-ductility and corrosion resistance. Compos, Part B Eng. 2022;234:109745. http://dx.doi.org/10.1016/j.compositesb.2022.109745.
28. Ettefagh AH, Zeng C, Guo S, Raush J. Corrosion behavior of additively manufactured Ti-6Al-4V parts and the effect of post annealing. Addit Manuf. 2019;28:252-8. http://dx.doi.org/10.1016/j.addma.2019.05.011.
29. Lek YZ, Wang C, Shen X, Chen Z, Ramamurty U, Zhou K. Additive manufacturing of corrosion-resistant maraging steel M789 by directed energy deposition. Mater Sci Eng A. 2022;857:144032. http://dx.doi.org/10.1016/j.msea.2022.144032.
30. Leon A, Levy GK, Ron T, Shirizly A, Aghion E. The effect of strain rate on stress corrosion performance of Ti6Al4V alloy produced by additive manufacturing process. J Mater Res Technol. 2020;9(3):4097-105. http://dx.doi.org/10.1016/j.jmrt.2020.02.035.
31. Sercombe TB, Zhang LC, Li S, Hao Y. Additive manufacturing of cp-Ti, Ti-6Al-4V and Ti2448. In: Froes FH, Qian M, editors. Titanium in medical and dental applications. Duxford: Elsevier; 2018. p. 303-24.
32. Soares FMS, Barbosa DM, Corado HPR, Santana AIC, Elias CN. Surface morphology, roughness, and corrosion resistance of dental implants produced by additive manufacturing. J Mater Res Technol. 2022;21:3844-55.
33. Turalıoğlu K, Taftalı M, Tekdir H, Çomaklı O, Yazıcı M, Yetim T et al. The tribological and corrosion properties of anodized Ti6Al4V/316L bimetallic structures manufactured by additive manufacturing. Surf Coat Tech. 2020;405:126635.
34. Wu B, Pan Z, Li S, Cuiuri D, Ding D, Li H. The anisotropic corrosion behaviour of wire arc additive manufactured Ti-6Al-4V alloy in 3.5% NaCl solution. Corros Sci. 2018;137:176-83. http://dx.doi.org/10.1016/j.corsci.2018.03.047.
35. Wu Y, Kuo C, Chung Y, Ng C, Huang JC. Effects of electropolishing on mechanical properties beam melting additive manufacturing. Materials. 2019;12(9):1466.
36. Bhardwaj T, Shukla M, Prasad NK, Paul CP, Bindra KS. Direct laser deposition-additive manufacturing of Ti–15Mo alloy: effect of build orientation induced surface topography on corrosion and bioactivity. Met Mater Int. 2020;26(7):1015-29. http://dx.doi.org/10.1007/s12540-019-00464-3.
37. Chandramohan P, Bhero S, Obadele BA, Olubambi PA. Laser additive manufactured Ti–6Al–4V alloy: tribology and corrosion studies. Int J Adv Manuf Technol. 2017;92(5-8):3051-61.
38. Chiu TM, Mahmoudi M, Dai W, Elwany A, Liang H, Castaneda H. Corrosion assessment of Ti-6Al-4V fabricated using laser powder-bed fusion additive manufacturing. Electrochim Acta. 2018;279:143-51. http://dx.doi.org/10.1016/j.electacta.2018.04.189.
39. Zhang D, Prasad A, Bermingham MJ, Todaro CJ, Benoit MJ, Patel MN et al. Grain refinement of alloys in fusion-based additive manufacturing processes. Metall Mater Trans, A Phys Metall Mater Sci. 2020;51(9):4341-59. http://dx.doi.org/10.1007/s11661-020-05880-4.
40. Naidoo LC, Fatoba OS, Akinlabi SA, Mahamood RM, Shatalov MY, Murashkin EV et al. Material characterization and corrosion behavior of hybrid coating Ti−Al−Si−Cu/Ti−6Al-4V composite. Materialwiss Werkstofftech. 2020;51(6):766-73.
41. Fujieda T, Chen M, Shiratori H, Kuwabara K, Yamanaka K, Koizumi Y et al. Mechanical and corrosion properties of CoCrFeNiTi-based high-entropy alloy additive manufactured using selective laser melting. Addit Manuf. 2019;25:412-20. http://dx.doi.org/10.1016/j.addma.2018.10.023.
42. Gai X, Bai Y, Li S, Wang L, Ai S, Hao Y et al. Review on corrosion characteristics of porous titanium alloys fabricated by additive manufacturing. J Shanghai Jiaotong Univ. 2021;26(3):416-30.
43. Lee J-B, Seo D-I, Chang H-Y. Evaluating corrosion resistance of biomedical Ti-6Al-4 V alloys fabricated via additive manufacturing using electrochemical critical localized corrosion potential. Met Mater Int. 2021;27(7):2353-9. http://dx.doi.org/10.1007/s12540-021-00972-1.
44. ASTM International. ASTM B962-13: standard test methods for density of compacted or sintered Powder Metallurgy (PM) products using Archimedes' principle. West Conshohocken: ASTM; 2013.
45. Haeri M, Haeri M, Image J. Plugin for analysis of porous scaffolds used in tissue engineering. J Open Res Softw. 2015;3:2-5.
46. Venkataraman R, Das G, Singh SR, Pathak LC, Ghosh RN, Venkataraman B et al. Study on influence of porosity, pore size, spatial and topological distribution of pores on microhardness of as plasma sprayed ceramic coatings. Mater Sci Eng A. 2007;445-446:269-74.
47. Luo Q, Yin L, Simpson TW, Beese AM. Effect of processing parameters on pore structures, grain features, and mechanical properties in Ti-6Al-4V by laser powder bed fusion. Addit Manuf. 2022;56:102915. http://dx.doi.org/10.1016/j.addma.2022.102915.
48. Montuori RAM, Figueira G, Cataldi TP, Alcântara NG, Bolfarini C, Coelho RT et al. Additive manufacturing of 316l stainless steel by selective laser melting. Soldag Insp. 2020;25:1-15.
49. Wang XJ, Zhang LC, Fang MH, Sercombe TB. The effect of atmosphere on the structure and properties of a selective laser melted Al-12Si alloy. Mater Sci Eng A. 2014;597:370-5.
50. Iveković A, Omidvari N, Vrancken B, Lietaert K, Thijs L, Vanmeensel K et al. Selective laser melting of tungsten and tungsten alloys. Int J Refract Met Hard Mater. 2018;72:27-32.
51. Gong H, Rafi K, Gu H, Starr T, Stucker B. Analysis of defect generation in Ti-6Al-4V parts made using powder bed fusion additive manufacturing processes. Addit Manuf. 2014;1:87-98. http://dx.doi.org/10.1016/j.addma.2014.08.002.
52. Promoppatum P, Srinivasan R, Quek SS, Msolli S, Shukla S, Johan NS et al. Quantification and prediction of lack-of-fusion porosity in the high porosity regime during laser powder bed fusion of Ti-6Al-4V. J Mater Process Technol. 2022;300:117426. http://dx.doi.org/10.1016/j.jmatprotec.2021.117426.
53. Khorasani AM, Gibson I, Awan US, Ghaderi A. The effect of SLM process parameters on density, hardness, tensile strength and surface quality of Ti-6Al-4V. Addit Manuf. 2019;25:176-86.
54. Javidrad HR, Salemi S. Effect of the volume energy density and heat treatment on the defect, microstructure, and hardness of L-PBF inconel 625. Metall Mater Trans, A Phys Metall Mater Sci. 2020;51(11):5880-91. http://dx.doi.org/10.1007/s11661-020-05992-x.
55. Yang J, Yu H, Yin J, Gao M, Wang Z, Zeng X. Formation and control of martensite in Ti-6Al-4V alloy produced by selective laser melting. Mater Des. 2016;108:308-18. http://dx.doi.org/10.1016/j.matdes.2016.06.117.
56. Zhou L, Yuan T, Tang J, He J, Li R. Mechanical and corrosion behavior of titanium alloys additively manufactured by selective laser melting – a comparison between nearly β titanium, α titanium and α + β titanium. Opt Laser Technol. 2019;119:105625. http://dx.doi.org/10.1016/j.optlastec.2019.105625.
57. Bandar A. Additive manufacturing of emerging materials. Cham: Springer; 2002.

58. Dai N, Zhang LC, Zhang J, Chen Q, Wu M. Corrosion behavior of selective laser melted Ti-6Al-4 V alloy in NaCl solution. Corros Sci. 2016;102:484-9.
59. Longhitano GA, Arenas MA, Conde A, Larosa MA, Jardini AL, Zavaglia CA C et al. Heat treatments effects on functionalization and corrosion behavior of Ti-6Al-4V ELI alloy made by additive manufacturing. J Alloys Compd. 2018;765:961-8.
60. Tshephe TS, Akinwamide SO, Olevsky E, Olubambi PA. Additive manufacturing of titanium-based alloys- a review of methods, properties, challenges, and prospects. Heliyon. 2022;8(3):e09041. http://dx.doi.org/10.1016/j.heliyon.2022.e09041.
61. Longhitano GA, Conde A, Arenas MA, Jardini AL, Zavaglia CAC, Maciel R Fo et al. Corrosion resistance improvement of additive manufactured scaffolds by anodizing. Electrochim Acta. 2021;366:137423. http://dx.doi.org/10.1016/j.electacta.2020.137423.
62. Damborenea JJ, Arenas MA, Larosa MA, Jardini AL, Zavaglia CAC, Conde A. Corrosion of Ti6Al4V pins produced by direct metal laser sintering. Appl Surf Sci. 2017;393:340-7. http://dx.doi.org/10.1016/j.apsusc.2016.10.031.